

Diagonal Waveform and Algorithm to Estimate Range and Velocity in Multi-Object Scenarios

Yi Geng
Cictmobile, China
gengyi@cictmobile.com

Abstract—Waveform design for joint communication and sensing (JCAS) is an important research direction, focusing on providing an optimal tradeoff between communication and sensing performance. In this paper, we first describe the conventional grid-type waveform structure and the corresponding two-dimension (2D)-discrete Fourier transform (DFT) algorithm. We then introduce an emerging diagonal scheme, including a diagonal waveform structure and corresponding 1D-DFT diagonal algorithm. The diagonal scheme substantially reduces the signaling overhead and computational complexity compared to the conventional 2D-DFT algorithm while still achieving the same radar performance. But the previous study of diagonal waveform used a single target to evaluate the performance of the diagonal scheme. This paper verifies the diagonal waveform with simulations demonstrating its feasibility in a traffic monitoring scenario with multiple vehicles.

Index Terms—OFDM, JCAS, radar, waveform design

I. INTRODUCTION

Joint communication and sensing (JCAS) is an emerging technology in 6G that localize and track passive targets or extract characteristics from targets (e.g., material information [1]) using wireless communication infrastructures. JCAS system needs to guarantee an appropriate radar performance by using the time-frequency resource shared between the communication and sensing functionalities. From a waveform design perspective, optimization of sensing signals, such as code sequence selection, modulation scheme, precoding, and power allocation, may conflict with the requirements of communication signals [2]. Therefore, dedicated sensing signals are desired. Waveform design for the JCAS system is formulated as an optimization problem to find a proper tradeoff between sensing and communication. For a fixed time-frequency resource block, the communication rate can be increased by degrading the radar performance and vice versa [3].

The sensing signals of orthogonal frequency division multiplexing (OFDM)-based JCAS systems can be allocated sparsely in the frequency and/or time domains to reduce sensing overhead, resulting in grid structures or comb structures. For example, an exemplary waveform in the grid structure is emitted for road traffic monitoring, as illustrated in Fig. 1. The transmitter of an OFDM-based JCAS system sends a time-frequency resource block with a bandwidth of 400 MHz and a duration of 30 ms consecutively. All the OFDM parameters used in this paper are listed in Table I. In the frequency domain, the sensing signals are transmitted every seven sub-

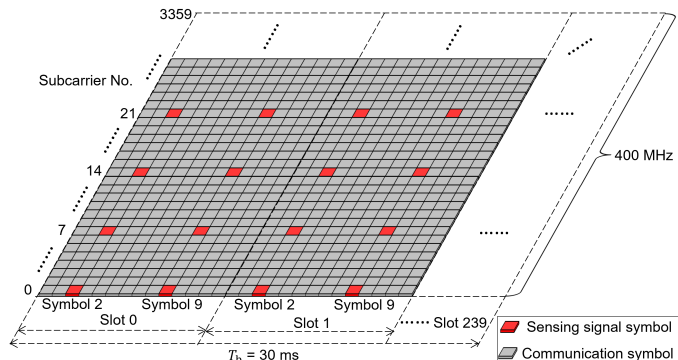


Fig. 1: A grid structure of sensing signals.

carriers. In the time domain, the sensing signals are transmitted every seven symbols. Therefore, there are 480 sensing signals (colored in red in Fig. 1) both in frequency and time domain in one resource block. The resources colored in gray are allocated for communication. According to the parameter dependencies of OFDM radar [4], the waveform in Fig. 1 would be sufficient to support a range resolution of 0.4 m, a velocity of 0.2 m/s, a maximum unambiguous detection range of 179 m, and a maximum unambiguous detection velocity of 92 m/s, which can meet the requirements of traffic monitoring applications. Assuming that the sensing blocks are transmitted consecutively, the sensing signal overhead of this waveform is 2%, which corresponds to the overhead for sensing in one beam direction. Considering that highly directional beams are needed to compensate for the high path loss at 28 GHz, the sensing beams must be emitted in many directions. Thus the sensing overhead increases further [5]. As a result, waveform structures with low overhead need to be developed.

The paper is structured as follows. Section II presents the conventional modulation-symbol-based OFDM radar processing algorithm. Section III presents an emerging diagonal waveform with low overhead and verify it in a single-target scenario. In Section IV, we extend the scheme in Section III to scenarios with multiple reflecting targets. Finally, the conclusions are drawn in Section V.

II. MODULATION-SYMBOL-BASED 2D-DFT ALGORITHM

One of the conventional algorithms for grid-type sensing signals, based on modulation-symbol, is employed to estimate the range and velocity of the reflecting objects [6]. The

TABLE I: OFDM parameters for 2D-DFT scheme and diagonal scheme

Parameter	Symbol	Value
Carrier frequency	f_c	28 GHz
Total signal bandwidth	B	400 MHz
Subcarrier spacing	Δf	120 KHz
OFDM symbol duration	T_{sym}	8.92 μs
Block duration	T_b	30 ms
Subcarriers in B	N_c	3360
Symbols in T_b	N_{sym}	3360
Sensing signals in B	N_f	480
Sensing signals in T_b	N_t	480
Sensing signals in diagonal	N	480

conventional algorithm is summarized in this section. The presence of reflecting objects in the detection range affects the propagation of radio waves in the air. The grid-type received sensing signal in the modulation symbol domain $\mathbf{c}_{\text{Rx}}(m, n)$, which consists of a superposition of the range and velocity information of the reflecting objects upon the transmitted sensing signal $\mathbf{c}_{\text{Tx}}(m, n)$ in the modulation symbol domain, is given by

$$\mathbf{c}_{\text{Rx}}(m, n) = A(m, n)\mathbf{c}_{\text{Tx}}(m, n)\phi_{\text{R}}(m) \otimes \phi_{\text{D}}(n), \quad (1)$$

where $\phi_{\text{R}}(m)$ is a $N_f \times 1$ vector, $\phi_{\text{D}}(n)$ is a $1 \times N_t$ vector, and

$$\phi_{\text{R}}(m) = \exp\left(\frac{-j4\pi\Delta f R m}{c}\right), m = 0, \dots, N_f - 1 \quad (2)$$

$$\phi_{\text{D}}(n) = \exp\left(\frac{j4\pi T_{\text{sym}} f_c v n}{c}\right), n = 0, \dots, N_t - 1 \quad (3)$$

where $A(m, n)$ represents the attenuation and phase shift due to the propagation and reflection, m is the individual subcarrier index from a total number of N_f subcarriers, n represents the individual OFDM symbol index within the total number of N_t symbols, \otimes referring to dyadic product, R is the range between the JCAS node and the reflecting object, v is the radial velocity of the reflecting object.

The normalized sensing signal matrix, $\mathbf{C}(m, n)$, can be obtained by element-wise division between $\mathbf{c}_{\text{Tx}}(m, n)$ and $\mathbf{c}_{\text{Rx}}(m, n)$, yielding a $N_f \times N_t$ matrix

$$\mathbf{C}(m, n) = \frac{\mathbf{c}_{\text{Rx}}(m, n)}{\mathbf{c}_{\text{Tx}}(m, n)} = A(m, n)\phi_{\text{R}}(m) \otimes \phi_{\text{D}}(n). \quad (4)$$

The linear phase shifts of the columns (or rows) of matrix $\mathbf{C}(m, n)$ contain the range (or Doppler) information of the target. Applying IDFT to vector $\phi_{\text{R}}(m)$, yielding

$$\Phi_r(p) = \text{IDFT}(\phi_{\text{R}}(m)) = \frac{1}{N_f} \sum_{m=0}^{N_f-1} \phi_{\text{R}}(m) \exp\left(\frac{j2\pi m p}{N_f}\right), \quad p = 0, \dots, N_f - 1 \quad (5)$$

The IDFT response $\Phi_r(p)$ shows a peak at IDFT bin index p_{peak} . Then the range R can be calculated by

$$R = \frac{c p_{\text{peak}}}{2\Delta f N_f}. \quad (6)$$

Similarly, applying DFT to vector $\phi_{\text{D}}(n)$, yielding

$$\Phi_v(q) = \text{DFT}(\phi_{\text{D}}(n)) = \sum_{n=0}^{N_t-1} \phi_{\text{D}}(n) \exp\left(-\frac{j2\pi n q}{N_t}\right), \quad q = 0, \dots, N_t - 1 \quad (7)$$

The DFT response $\Phi_v(q)$ shows a peak at DFT bin index q_{peak} . Then the velocity v can be calculated by

$$v = \frac{c q_{\text{peak}}}{2f_c T_{\text{sym}} N_t}. \quad (8)$$

In practice, 2D-DFT of matrix $\mathbf{C}(m, n)$ is performed to derive the range and velocity of the reflecting object simultaneously. 2D-DFT of $\mathbf{C}(m, n)$ is equivalent to column-by-column 1D-IDFTs of length N_f after row-by-row 1D-DFTs of length N_t .

III. A DIAGONAL WAVEFORM DESIGN AND CORRESPONDING ALGORITHM

From the implementation point of view, the high computational complexity of large-scale DFT/IDFT calculations creates a bottleneck and limits the sensing performance of the 2D-DFT algorithm [7]. To derive a range-velocity measurement from a $N \times N$ modulation symbol matrix $\mathbf{C}(m, n)$, $2N\mathcal{O}(N^2)$ complex multiplications are needed, including N DFTs on N rows and N IDFTs on N columns. In addition, the grid structure incurs a large sensing signal overhead and degraded communication performance.

To tackle these problems, we have proposed a diagonal waveform structure, and corresponding diagonal algorithm for single-target scenario in our previous work [8]. The scheme in [8] is as follows. The JCAS system uniformly allocates the sensing signals along the resource block diagonal and reserves the resources outside the diagonal for communication. This structure guarantees that the same number of sensing signals, N , is transmitted both in frequency band B and in time duration T_b . As depicted in Fig. 2(a), the transmitter emits one block of radio signals, including 480 sensing signals along the diagonal of the block and user data for communication. To ensure target tracking, the diagonal signals are emitted every 30 ms, as shown in Fig. 2(b). The normalized sensing signal vector, $\mathbf{d}(k)$, can be acquired by exploiting transmitted sensing signal vector $\mathbf{d}_{\text{Tx}}(k)$ and the received echos $\mathbf{d}_{\text{Rx}}(k)$, yielding

$$\begin{aligned} \mathbf{d}(k) &= \frac{\mathbf{d}_{\text{Rx}}(k)}{\mathbf{d}_{\text{Tx}}(k)} \\ &= A(k) \exp\left(\frac{-j4\pi\Delta f R k}{c}\right) \exp\left(\frac{j4\pi T_{\text{sym}} f_c v k}{c}\right), \quad k = 0, \dots, N - 1 \end{aligned} \quad (9)$$

where $A(k)$ represents the attenuation and phase shift due to the propagation and reflection, and

$$\phi_{\text{R}}(k) = \exp\left(\frac{-j4\pi\Delta f R k}{c}\right), \quad (10)$$

$$\phi_{\text{D}}(k) = \exp\left(\frac{j4\pi T_{\text{sym}} f_c v k}{c}\right). \quad (11)$$

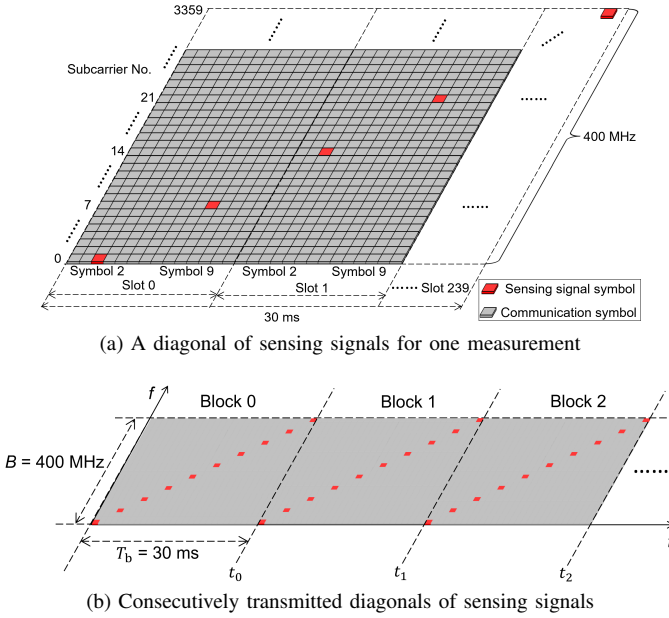


Fig. 2: The diagonal structure of sensing signals.

The modulation symbol vector $\mathbf{d}(k)$ simultaneously incorporates the phase shifts induced by the range R and the velocity v because the diagonal signals span both the frequency and time domains. Therefore, the range and velocity of the objects can be derived simultaneously by performing DFT to $\mathbf{d}(k)$, which yields

$$\Phi_{rv}(l) = \text{DFT}(\mathbf{d}(k)) = \sum_{k=0}^{N-1} \phi_R(k) \phi_D(k) \exp(-\frac{j2\pi kl}{N}),$$

$$l = 0, \dots, N-1 \quad (12)$$

The DFT of $\mathbf{d}(k)$ generates a dual-peak-like profile. Fig. 3 illustrates the dual-peak profile caused by an object with range $R = 40$ m and velocity $v = 5$ m/s by using the diagonal waveform and 1D-DFT diagonal algorithm. The dual-peak profile indicates two peaks at the DFT bin indices $l_1 = 81$ and $l_2 = 134$. A new term l_{mean} is defined as the mean of the peak bin indices l_1 and l_2 . Another term, l_{Δ} , is defined as the difference between the peak bin indices l_2 and l_1 . The terms l_{mean} and l_{Δ} are given by

$$l_{\text{mean}} = \frac{l_1 + l_2}{2}, \quad (13)$$

$$l_{\Delta} = l_2 - l_1. \quad (14)$$

One of l_{mean} and l_{Δ} incorporates the range information, whereas the other incorporates the velocity information. The range R and velocity v of the object can be calculated by

$$R = \frac{cl_{\text{mean}}}{2\Delta f N_c}, v = \frac{cl_{\Delta}}{4T_{\text{sym}} f_c N_c}, \quad (15)$$

or

$$R = \frac{cl_{\Delta}}{4\Delta f N_c}, v = \frac{cl_{\text{mean}}}{2T_{\text{sym}} f_c N_c}. \quad (16)$$

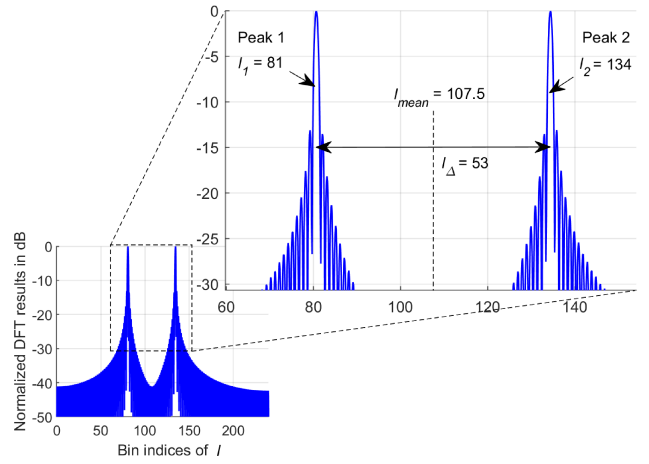


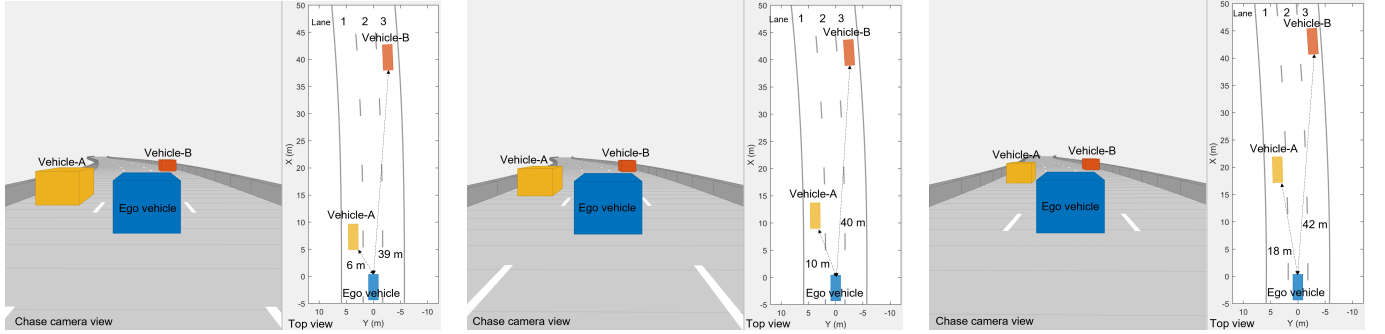
Fig. 3: The radar image of an object with range of 40 m and velocity of 5 m/s using the diagonal waveform and corresponding 1D-DFT diagonal algorithm.

However, either (15) or (16) returns unexpected range-velocity values because of the unlabeled bin indices l_1 and l_2 . We are uncertain which equation among (15) and (16) is indicative of the accurate range and velocity. For the case shown in Fig. 3, by using (15), $R = 40$ m and $v = 5$ m/s can be derived. Or by using (16), $R = 10$ m and $v = 20$ m/s is obtained. This means that a target with $R = 40$ m and $v = 5$ m/s induces the same dual-peak profile as that of another target with $R = 10$ m and $v = 20$ m/s. How to resolve this ambiguity has been discussed in [8].

IV. PERFORMANCE ANALYSIS FOR MULTI-OBJECT SCENARIO

Our previous work in [8] used a single target to evaluate the performance of the diagonal algorithm but did not verify its performance in multi-object scenarios. However, the typical scenarios, e.g., the automotive environment, consists of multiple objects. When applying the diagonal scheme to the multi-object scenario, additional problems arise, including:

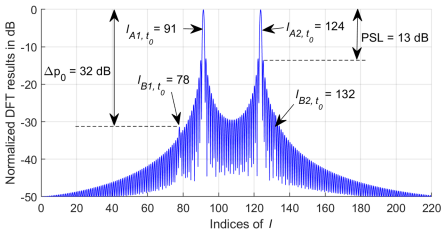
- In the radar image, the amplitudes of the peaks induced by objects are determined by their radar cross sections (RCSs) and distances. The peak caused by a weak target (e.g., a tiny target or a target at a long distance) might be overshadowed by the sidelobes caused by a strong target (e.g., a large target or a target at close range). This problem reduces the probability of detection for weak targets.
- Using the diagonal algorithm, two objects with different ranges and velocities may induce the same dual-peak profile. Unlabeled two peaks from a dual-peak profile in the radar image cause this ambiguity.
- Each range-velocity estimate is derived from the two peaks caused by one object. The peaks in a radar image must be paired before applying the diagonal algorithm in multi-object scenarios.



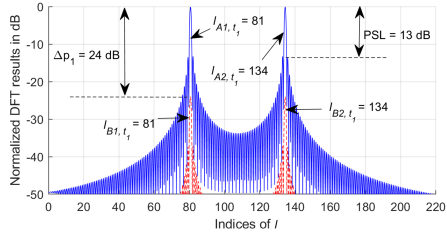
(a) Snapshot captured at time $t_0 = 0$ s, showing a yellow car traveling 6 m ahead on the left lane and a red car traveling 39 m ahead on the right lane

(b) Snapshot captured at time $t_1 = 0.2$ s, showing a yellow car traveling 10 m ahead on the left lane and a red car traveling 40 m ahead on the right lane

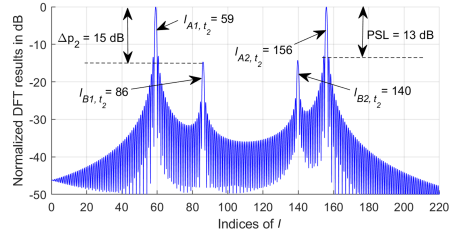
(c) Snapshot captured at time $t_2 = 0.6$ s, showing a yellow car traveling 18 m ahead on the left lane and a red car traveling 42 m ahead on the right lane



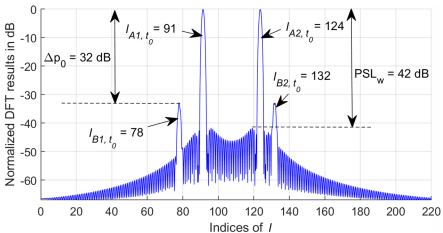
(d) The radar image calculated at time $t_0 = 0$ s, vehicle-A with $R = 6$ m and $v = 20$ m/s, and vehicle-B with $R = 39$ m and $v = 5$ m/s, no windowing



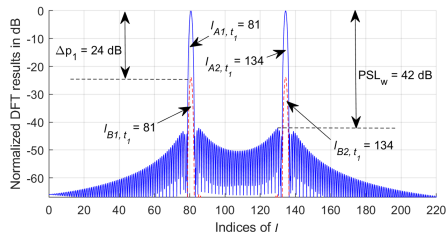
(e) The radar image calculated at time $t_1 = 0.2$ s, vehicle-A with $R = 10$ m and $v = 20$ m/s, and vehicle-B with $R = 40$ m and $v = 5$ m/s, no windowing



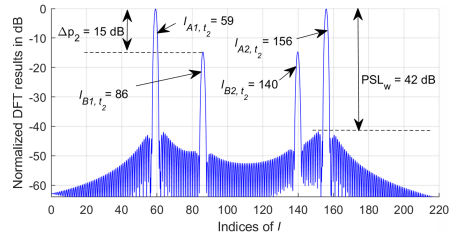
(f) The radar image calculated at time $t_2 = 0.6$ s, vehicle-A with $R = 18$ m and $v = 20$ m/s, and vehicle-B with $R = 42$ m and $v = 5$ m/s, no windowing



(g) The radar image calculated at time $t_0 = 0$ s, vehicle-A with $R = 6$ m and $v = 20$ m/s, and vehicle-B with $R = 39$ m and $v = 5$ m/s, with Hamming window applied



(h) The radar image calculated at time $t_1 = 0.2$ s, vehicle-A with $R = 10$ m and $v = 20$ m/s, and vehicle-B with $R = 40$ m and $v = 5$ m/s, with Hamming window applied



(i) The radar image calculated at time $t_2 = 0.6$ s, vehicle-A with $R = 18$ m and $v = 20$ m/s, and vehicle-B with $R = 42$ m and $v = 5$ m/s, with Hamming window applied

Fig. 4: A simulated highway scenario and the radar images obtained by the ego vehicle using the proposed algorithm.

To present our solutions for the above problems, we simulate a highway scenario with multiple vehicles and generate detections using the diagonal algorithm. As shown in Fig. 4, the scenario consists of a blue ego car with sensor and two cars to be detected, colored orange and red, respectively. All vehicles have identical RCS $\sigma = 5$ dBm². The ego car travels along the highway's center lane at a constant velocity of 20 m/s. At time $t_0 = 0$ seconds, the orange car, which is labeled as vehicle-A, is moving 6 meters ahead of the ego vehicle at a constant velocity of 40 m/s along the left lane, while the red car (vehicle-B) is traveling 39 m in front of the ego car at a constant velocity of 25 m/s along the right lane. Figs. 4(a)-(c) illustrate the snapshots of this highway scenario captured at time $t_0 = 0$ seconds, $t_1 = 0.2$ seconds, and $t_2 = 0.6$ seconds, respectively, showing the situation in

front of the ego car using chase camera view and top view.

The ego car is equipped with a forward-looking antenna that simultaneously provides communication and range-velocity sensing coverage. Angle estimation is not considered in this paper. Fig. 4(d) is derived from the measurement at time $t_0 = 0$ seconds using the diagonal algorithm. The two dual-peak profiles resulting from vehicle-A and vehicle-B are superimposed. However, only the two peaks, l_{A1,t_0} and l_{A2,t_0} , caused by vehicle-A, are sharply depicted. The peaks caused by vehicle-B (l_{B1,t_0} and l_{B2,t_0}) are overshadowed by the sidelobes caused by vehicle-A. The amplitude of the peak in the radar image relates to the received signal power P_R reflected by the object. P_R is given by [9]

$$P_R = \frac{P_{Tx} G_{Tx} G_{Rx} \sigma \lambda^2}{(4\pi)^3 R^4 f_c^2}, \quad (17)$$

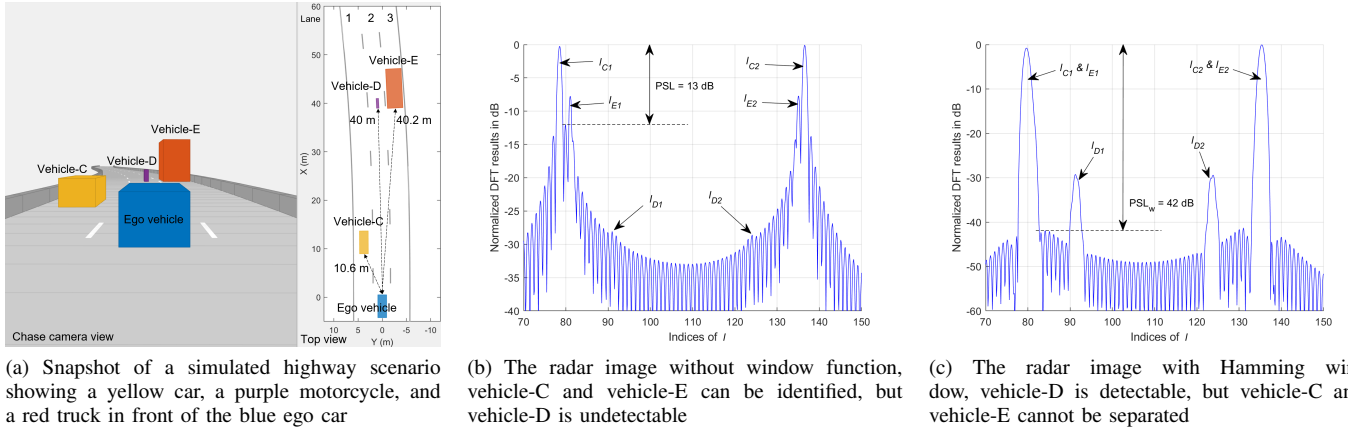


Fig. 5: A simulated highway scenario and the radar images obtained by the ego vehicle using the proposed algorithm.

where P_{Tx} is the transmitted power, G_{Tx} is the antenna gain at Tx, G_{Rx} is the antenna gain at Rx, σ is the RCS of the object, λ is the wavelength of the carrier, R is the distance between the antenna and the object.

From (17), the received signal power P_R is dependent on range R . The return signal from a close target is stronger than the return signal from a target farther away if they have identical RCS. According to their distances, the received signal power from vehicle-A is 32 dB higher than the received signal power from vehicle-B. This results in the fact that the amplitudes of peak l_{A1,t_0} and l_{A2,t_0} caused by vehicle-A are 32 dB higher than the amplitudes of peaks l_{B1,t_0} and l_{B2,t_0} caused by vehicle-B. Peak l_{B2,t_0} is totally overshadowed by the sidelobes caused by vehicle-A, and peak l_{B1,t_0} is almost indistinguishable. Therefore, vehicle-B cannot be detected. This exhibits that the dynamic range of the JCAS system is limited by the sidelobes of the Fourier transform when close targets or large targets exist in the detection area.

In the discrete-time signal process, Hamming windowing is a signal shaping technique, usually applied to mitigate the impact of sidelobes of DFT [10]. Fig. 4(g) shows the radar image derived from the scenario illustrated in Fig. 4(a) with the diagonal algorithm and with Hamming window. Compared to Fig. 4(d), the peak-to-sidelobe level (PSL) with Hamming window PSL_w is reduced from -13 dB to -42 dB. With the help of Hamming window, peaks l_{B1,t_0} and l_{B2,t_0} caused by vehicle-B now clearly stand out against the well-suppressed sidelobes induced by vehicle-A.

Fig. 4(e) and Fig. 4(h) illustrate the radar images derived by the ego car at time $t_1 = 0.2$ seconds without and with Hamming window, respectively. A red dashed line indicates the dual-peak profile caused by vehicle-B for clear visualization. As displayed, the bin positions of peaks l_{A1,t_1} and l_{A2,t_1} coincide with the bin positions of peaks l_{B1,t_1} and l_{B2,t_1} . This is the ambiguity mentioned in Section III, i.e., two objects with different ranges and velocities may induce the same dual-peak profile. Range and velocity of vehicle-A and vehicle-B cannot be determined only by the superimposed dual-peak profiles derived at time t_1 . However, variations in range and

velocity cause time-varying peak amplitude and peak bin index in the radar image. Therefore, the fusion of estimates acquired at various times can resolve the ambiguity. For example, according to the different peak patterns of vehicle-A and vehicle-B at time t_0 , the range-velocity estimates derived at time t_0 can assist the JCAS system in estimating the range-velocity of vehicle-A and vehicle-B when ambiguity occurs at time t_1 . How to resolve this ambiguity is analyzed in greater detail in our previous work [8].

As illustrated in Figs. 4(a)-(c), vehicle-A is approaching vehicle-B due to its higher velocity than the velocity of vehicle-B. Therefore, the difference between the received signal powers from both vehicles is decreasing. As shown in Fig. 4(f), at time $t_2 = 0.6$ seconds, the peaks induced by vehicle-B (l_{B1,t_2} and l_{B2,t_2}) stand out against the sidelobes caused by vehicle-A, even though Hamming window is not applied. This is because the sidelobes caused by vehicle-A are not higher than peaks l_{B1,t_2} and l_{B2,t_2} any longer due to the similar signal returns from both vehicles. The amplitude difference between peaks caused by the two vehicles Δp_2 reduces to 15 dB only.

From Figs. 4(d)-(i), it can be concluded that weak targets might be overshadowed when strong targets are in the detection range. A window with high sidelobe attenuation can be used to mitigate this issue. However, it reduces the “peak resolution” of the diagonal algorithm. It is worth mentioning that peak resolution here differs from the radar’s definition of range resolution (or velocity resolution). The bin index of a peak obtained by the diagonal algorithm is mixed with the range and velocity information of the object. Hence, two objects with vastly different ranges (or velocities) may induce peaks close to each other. Peak resolution is the capability of the diagonal algorithm to distinguish adjacent peaks caused by two objects in the radar image.

We investigate the performance of the diagonal algorithm with and without applying Hamming window in a simulated highway scenario shown in Fig. 5(a). The scenario consists of two strong scatterers and one weak scatterer, which are an orange car (vehicle-C, strong scatterer) with a small RCS of

5 dBm² close to the ego car, a purple motorcycle (vehicle-D, weak scatterer) with a small RCS of 1 dBm² far away from the ego car, and a red truck (vehicle-E, strong scatterer) with a large RCS of 100 dBm² far away from the ego car. Vehicle-C is moving 10.6 m ahead of the blue ego car at a relative velocity of 20 m/s on the left lane. Vehicle-D is traveling 40 m in front of the ego car on the same lane at a relative velocity of 3 m/s. Vehicle-E, 40.2 m away from the ego car, is moving at a relative velocity of 5 m/s on the right lane.

Fig. 5(b) shows the radar image derived by the ego vehicle using the diagonal algorithm. Vehicle-C causes peaks l_{C1} and l_{C2} , and vehicle-E causes peaks l_{E1} and l_{E2} . Although the truck is far away from the ego car, the return signal from the truck is only 8 dB weaker than the return signal from the strongest scatterer (vehicle-C) thanks to the large RCS of the truck. Peaks l_{E1} and l_{E2} can still stand out against the unsuppressed sidelobes caused by vehicle-C. Vehicle-C and vehicle-E cause peaks close to each other. However, the diagonal algorithm without window function has high peak resolution due to the narrow mainlobes in the radar image. The peaks caused by vehicle-C and vehicle-E can be clearly separated. The weak scatterer (vehicle-D) has a small RCS and is far from the radar. Thus, the return signal from the motorcycle is 30 dB weaker than that from vehicle-C. The peaks caused by the motorcycle, l_{D1} and l_{D2} , are almost indistinguishable in the radar image.

Fig. 5(c) illustrates the radar image produced by the diagonal algorithm with Hamming window. One can see that the sidelobes of peaks caused by the strong scatterer are well suppressed but at the cost of lower peak resolution. The peaks caused by the weak scatterer, l_{D1} and l_{D2} , can be detected. However, as a result of Hamming window, the peaks caused by vehicle-C and vehicle-E are widened and they cannot be separated in the radar image.

We suggest an adaptive window strategy, e.g., a time multiplexing window strategy, to ensure both the peak resolution and detection of weak objects when designing a JCAS system. Window function needs to be applied according to the distribution of the objects in the detection range. Peak resolution is essential if the radar image contains two or more peaks near to each other and the peaks have similar amplitudes. In this case, it is best to sense the objects without applying any window function. A window function should be used if there is a large gap between the return signal power from different objects.

Another problem with the diagonal algorithm is peak pairing. The algorithm uses the pairwise peaks caused by one object to derive its range and velocity. However, the dual-peak profiles caused by multiple objects are superimposed, producing a radar image with more peaks than the number of objects. Consequently, the diagonal algorithm cannot be directly applied. For example, as shown in Fig. 4(i), vehicle-A and vehicle-B induce four peaks in the radar image. The four peaks must be paired such that the peaks in each pair are caused by one object before applying the diagonal algorithm. A simple solution to this problem is to compare the amplitudes of all peaks in the radar image. According to (17), the two

peaks caused by one object have the same amplitude. Thus, it can be concluded that one vehicle causes peaks $l_{A1,t2}$ and $l_{A2,t2}$, and another vehicle causes peaks $l_{B1,t2}$ and $l_{B2,t2}$.

V. CONCLUSIONS

A diagonal waveform and corresponding 1D-DFT diagonal algorithm for the JCAS system was proposed in [8]. Compared to the grid waveform structure in Fig. 1, the overhead of the diagonal waveform in Fig. 2 reduces from N^2/N_c^2 to N/N_c^2 . Furthermore, the computational complexity of one estimation is reduced from $2N \times \mathcal{O}(N^2)$ to $\mathcal{O}(N^2)$. However, the diagonal algorithm in [8] was only verified for single object scenarios. In this paper, We simulate a highway scenario including multiple vehicles with different ranges, velocities, and RCSs. We then demonstrate that the diagonal algorithm can be extended to range-velocity estimation for multi-object scenarios. A new concept “peak resolution” and some design strategies for the diagonal algorithm are also presented.

VI. ACKNOWLEDGMENT

This work has been funded by the National Key Research and Development Program of China (No.2021YFB2900200).

REFERENCES

- [1] Y. Geng, V. Yajnanarayana, A. Behravan, E. Dahlman, and D. Shrestha, “Study of reflection-lass-based material identification from common building surfaces,” in *2021 Joint European Conference on Networks and Communications & 6G Summit (EuCNC/6G Summit)*, 2021, pp. 526–531.
- [2] H. Li, “Conflict and trade-off of waveform uncertainty in joint communication and sensing systems,” in *ICC 2022 - IEEE International Conference on Communications*, 2022, pp. 5561–5566.
- [3] F. Liu, Y. Cui, C. Masouros, J. Xu, T. X. Han, Y. C. Eldar, and S. Buzzi, “Integrated sensing and communications: Toward dual-functional wireless networks for 6g and beyond,” *IEEE Journal on Selected Areas in Communications*, vol. 40, no. 6, pp. 1728–1767, 2022.
- [4] T. Wild, V. Braun, and H. Viswanathan, “Joint design of communication and sensing for beyond 5G and 6G systems,” *IEEE Access*, vol. 9, pp. 30 845–30 857, 2021.
- [5] A. Behravan, R. Baldemair, S. Parkvall, E. Dahlman, V. Yajnanarayana, H. Björkegren, and D. Shrestha, “Introducing sensing into future wireless communication systems,” in *2022 2nd IEEE International Symposium on Joint Communications & Sensing (JC&S)*, 2022, pp. 1–5.
- [6] C. Sturm, M. Braun, and Z. Thomas, “Spectrally interleaved multi-carrier signals for radar network applications and multi-input multi-output radar,” *IET Radar, Sonar and Navigation*, vol. 7, no. 3, pp. 261–269, 2012.
- [7] Y. Ouerhani, M. Jridi, and A. Alfalou, “Implementation techniques of high-order FFT into low-cost fpga,” in *2011 IEEE 54th International Midwest Symposium on Circuits and Systems (MWSCAS)*, 2011, pp. 1–4.
- [8] Y. Geng, “A novel waveform design for OFDM-based joint sensing and communication system,” in *2023 IEEE 3rd International Symposium on Joint Communications & Sensing (JC&S)*, 2023, pp. 1–6.
- [9] M. Braun, C. Sturm, and F. K. Jondral, “On the single-target accuracy of ofdm radar algorithms,” in *2011 IEEE 22nd International Symposium on Personal, Indoor and Mobile Radio Communications*, 2011, pp. 794–798.
- [10] F. Harris, “On the use of windows for harmonic analysis with the discrete fourier transform,” *Proceedings of the IEEE*, vol. 66, no. 1, pp. 51–83, 1978.